

**Numerical Modelling of Tidally-Driven Fractures  
Interacting with Meltwater Lenses on the Surface of  
Europa**

**John C. N. W. Walding<sup>1</sup>, Adriana Paluszny<sup>1</sup> and Robert W. Zimmerman<sup>1</sup>**

<sup>1</sup>Imperial College London, Department of Earth Sciences and Engineering

**Key Points:**

- Three-dimensional simulations of the Europan surface systematically quantify fracturing with varying location, orientation, and latitude
- The growth of fractures is quantified for homogeneous domains and for domains that contain subsurface meltwater lenses
- Subsurface meltwater lenses create mechanical conditions leading to fracture and fragmentation, conducive to chaos terrain formation

---

Corresponding author: John Walding, [jcw15@ic.ac.uk](mailto:jcw15@ic.ac.uk)

13      **Abstract**

14      The ice crust of Jupiter's Galilean satellite Europa exhibits a number of large-scale lineae features, as well as numerous regions with smaller-scale lineae patterns and chaos features. In this work, a three-dimensional finite element simulator is used to model lineae as fractures in the crust that nucleate, grow, and interact. The growth of fractures is modelled geometrically as a function of multi-modal stress intensity factors computed at the fracture tips, and the tidal forces that drive this fracturing process are computed according to a closed-form satellite tidal stress model. Fracture growth is modelled across the span of the satellite, with emphasis on analysing fracture statistics in the tropical region around 30° North at various longitudes. Specific focus is given to fracture behaviour in the presence of subsurface meltwater lenses. The effect that these lenses have upon fracture development is systematically investigated in order to determine whether a subsurface lens may catalyse the development of chaos terrain on the surface. The results show a dependence on longitude, with the most pronounced effects seen around the sub-jovian point (0°), 90°E, 180°E and 270°E, which correspond to the regions of greatest change in the stress field. In most regions, the observed behaviour of fractures in proximity to a lens correlates with the hypothesis that lenses lead to chaos formation.

30      **Plain Language Summary**

31      Europa is the fourth largest moon of Jupiter, and it is encased within an ice crust approximately 25 km thick. Between the rock and ice is believed to be a liquid water ocean approximately 100 km deep. This ocean is one of the prime candidates for possible extraterrestrial life within the solar system, and therefore the ocean and Europa as a whole are of great interest to the scientific community. The outer surface of the ice also shows a number of linear features called lineae, believed to be either fractures or former fractures, as well as rugged and broken up areas called chaos. These fractures and their behaviour, especially in the context of chaos, are the focus of research for this work. The work consists of calculating tidal stresses imparted on Europa by Jupiter using a satellite stress model, and then using these stresses to drive fracture behaviour within the ice crust, modelled using a numerical simulator. Some simulations also contain a subsurface meltwater lens. The results from the simulations are analysed in the context of how fracturing and lineae in the vicinity of a subsurface meltwater lens behave. The results indicate that subsurfaces lenses may contribute to the formation of chaos terrain.

## 45 1 Introduction

46 The four largest moons of Jupiter were first observed by Galileo in 1610, and there-  
 47 after have been known as the Galilean moons. The smallest of the Galilean moons, Eu-  
 48 ropa, became the subject of scientific curiosity when modern imaging revealed that it  
 49 was entirely encased within an ice crust estimated to be between 1 and 30 km thick (Bills,  
 50 2005). The lower bound on the thickness is determined by mechanical flexure analyses  
 51 (Figueiredo et al., 2002; Nimmo et al., 2007), and the upper bound from thermodynamic  
 52 analyses (Hussmann et al., 2002; McKinnon, 1999; Ojakangas & Stevenson, 1989b), with  
 53 impact cratering analyses yielding estimates between these bounds (Greeley et al., 1998;  
 54 Moore et al., 1998; Schenk, 2002).

55 Interest in Europa grew when considerations of tidal heating implied the existence  
 56 of a vast subsurface ocean between the silicate core and icy crust (Cassen et al., 1979),  
 57 with this conclusion supported by the results from the Galileo mission (Carr et al., 1998).  
 58 This ocean, thought to be approximately 100 km thick (Pappalardo et al., 1999), may  
 59 be the prime candidate for extra-terrestrial life within the solar system (Schulze-Makuch  
 60 & Irwin, 2001; Kargel et al., 2000; Greenberg et al., 2000) and therefore understanding  
 61 the ocean-crust system of Europa is of importance.

62 Current observational knowledge of Europa is limited due to its distance from Earth.  
 63 The planned Europa Clipper (Bayer et al., 2019) and JUICE (Witasse, 2020) missions  
 64 are expected to significantly improve the quality and quantity of Europan observational  
 65 data, but in their absence the dataset is limited to the images and data yielded by NASA  
 66 missions Pioneer 10 and 11, Voyager 1 and 2, Galileo, New Horizons, and Juno. The re-  
 67 turned images of the visible ice crust reveal many types of geomorphological feature, of  
 68 which two broad categories are investigated in this work; regions of broken and jagged  
 69 terrain called *chaos* (Collins & Nimmo, 2009), and *lineae*, line-like features that exist across  
 70 many length-scales and are thought to be either active or healed fractures in the ice crust  
 71 (Helfenstein & Parmentier, 1983).

72 The presence of fractures in the form of *lineae* is thought to be possible due to the  
 73 presence of the subsurface ocean (Pappalardo et al., 1999; Carr et al., 1998), where the  
 74 main driving stress on the ice crust causing the fracturing is the tidal influence from the  
 75 interaction of Europa with its parent body, Jupiter (Greenberg et al., 1998; Hoppa et  
 76 al., 1999). The study performed by Mondro et al. (2023) categorised a subset of the Eu-  
 77 ropan *lineae* showing that their lengths can be described by a power law, although the  
 78 present imaging quality is insufficient to resolve the smaller fractures in most regions,  
 79 as only 32% of the surface is imaged with a quality of 1 km pixel<sup>-1</sup> or better (Bland et  
 80 al., 2021; Greeley et al., 2000), and therefore the power law is extracted from the larger  
 81 observed *lineae*. A computational study of these fractures would aid with understand-  
 82 ing the presently unseen behaviour of the ice crust.

83 Previously, Linear Elastic Fracture Mechanics (LEFM) methods have been used  
 84 to model fracturing in the Europan crust, for example Marshall and Kattenhorn (2005),  
 85 Lee et al. (2005), Craft et al. (2016) and Poinelli et al. (2019). The work undertaken by  
 86 Marshall and Kattenhorn (2005) and Poinelli et al. (2019) concern cycloidal *lineae*; Marshall  
 87 and Kattenhorn (2005) showed that these features are driven by diurnal tidal stressors  
 88 while emphasising the role shear stresses play in cycloid formation while Poinelli et al.  
 89 (2019) concludes that dormant growth periods may account for cycloid development. Craft  
 90 et al. (2016) considered the formation of subsurface water sills as a result of surface and  
 91 basal fracture propagation, taking into account shell cooling and thickening as shell stress-  
 92 sors in two dimensions, showing that horizontal stresses appear to be insufficient to turn  
 93 fractures to form sills.

94 Lee et al. (2005) investigated the vertical propagation of surface fractures, conclud-  
 95 ing that, assuming the presence of a subsurface ocean, surface tidally driven fractures

may penetrate the entirety of the Europan crust. This conclusion was however disputed by Qin et al. (2007), where it was posited that normal stresses acting upon the fractures were not considered and in this revised formulation the fractures may no longer penetrate to the ocean (this in turn was replied to by Lee et al. (2007)). Further work on vertical propagation was conducted by Rudolph and Manga (2009) and Walker et al. (2021) using a boundary element method and theoretical quasi-static LEFM respectively. Both predict that it is unlikely that fractures would penetrate the whole crust due to lithostatic overburden, Rudolph and Manga (2009) stating that penetration is only likely if the crust is 2.5 km thick or thinner, which is less than most current estimates.

A theory pertaining to the formation of chaos morphologies on the surface is that they are the consequence of subsurface meltwater sills or lenses (Collins et al., 2000; O'Brien et al., 2002; Schmidt et al., 2011). Pockets of fluids are expected to form directly beneath the ice surface, these meltwater pockets are the result of localised melting due to tidal flexing. Numerical models have suggested that these isolated meltwater pockets are likely to develop in depths of up to 5km, in particular for a hypothesis of ice shelf thickness between 15–35 km (Vilella et al., 2020). This is further supported by a hypothesis of the presence of brine on Europa's surface (Sieme & Rezaei-Ghaleh, 2024), which would lower the freezing point of water, facilitating the formation of lenses. The proposed mechanism for chaos formation relies on fracturing from the shallow lens to the surface to allow for water to float the observed ice “rafts” in the terrain (Becker et al., 2023). Such lenses may be observable by the upcoming Europa Clipper and JUICE missions (Heggy et al., 2017; Di Paolo et al., 2022), though in the interim the distribution of these saltwater lenses is not well known. Alternative formation mechanisms have been proposed, for example by Howell et al. (2021) where dry porous compaction is used to explain chaos formation, and therefore eliminating the need for subsurface meltwater. However, in all proposed mechanisms, there must be more contribution than solely tidal forcing due to the irregular distribution of chaos across the surface, as opposed to the regular predictable concentrations if tidal stresses alone were sufficient.

The present research seeks to build on these works by increasing the computational detail applied to the fractures and the domain, using an existing geologic fracture simulator. The primary objective is to systematically study the behaviour of fractures on the surface and more specifically to investigate the interaction of fractures with subsurface meltwater lenses, and whether this interaction may contribute to the formation and evolution of chaos terrain. This study is executed through modelling of the growth of Europan surface lineae as a result of tidal forcing from Jupiter, assuming that the lineae can be described by a first principles discrete fracture mechanics growth model that combines damage and energy-based modelling of fracture growth.

## 2 Methodology

In this work the term “fractures” refers in the most generic sense to discontinuities in the solid mass of the Europan crust, which may be open or closed, and may progressively accrue surface area in response to mechanical effects.

### 2.1 Tidal Stress Model

It is believed that the principal driving force for the development of lineae on the Europan surface are the tidal stresses exerted by Europa's interaction with Jupiter (Helfenstein & Parmentier, 1983), and are therefore implemented as the driving factor behind fracture growth in this work, where the primary tidal stressors are diurnal stresses and Non-Synchronous Rotation (NSR) stresses. While further sources of stress have been theorised, such as orbital obliquity by Bills (2005) or librational tides by Van Hoolst et al. (2008), these are taken to be second order effects (Wahr et al., 2009) and not considered.

145 Diurnal stresses are resultant from the eccentricity of Europa's orbit about Jupiter,  
 146 yielding a stress field on the order of 100 kPa that fluctuates over the course of a Eu-  
 147 ropan day (3.5 Earth days), where the rate of rotation is referred to as  $n$ . NSR arises  
 148 due to the mechanical decoupling of the ice crust from the silicate core as a result of the  
 149 ocean, allowing the ice crust to rotate at a different rate than that of the tidally-locked  
 150 core (Geissler et al., 1998). The additional rotation due to NSR is  $b$ , such that the over-  
 151 all rotation of the moon is  $n + b$ . Due to the lack of tidal lock, the tidal bulge moves  
 152 with respect to the ice crust therefore exerting stress upon the ice. The magnitude of  
 153 the NSR stress depends on both the viscosity of ice and the NSR period, taking values  
 154 from 0 MPa to 3 MPa. Further detail on the NSR is given in Section 3.1.

### 155 2.1.1 Tidal Stress Model Implementation

156 The tidal stresses are calculated using a model based upon the theory developed  
 157 by Wahr et al. (2009). This model starts from the fundamental gravitational potential  
 158 to derive analytical expressions for the tidal stress exerted on the surface. The expres-  
 159 sions are parametrised by the location and time, with time measured from Europen pe-  
 160 riapsis (the closest approach of Europa to Jupiter). The gravitational potential,  $V_T$ , is  
 161 given by

$$V_T(r, \theta, \phi, t) = Z \left( \frac{r}{R_s} \right)^2 [T_* + T_0 + T_1 + T_2] \quad (1)$$

162 with

$$T_* = \frac{1}{6}(1 - 3\cos^2\theta), \quad (2)$$

$$T_0 = \frac{1}{2}\sin^2\theta\cos(2\phi + 2bt), \quad (3)$$

$$T_1 = \frac{\epsilon}{2}(1 - 3\cos^2\theta)\cos(nt), \quad (4)$$

$$T_2 = \frac{\epsilon}{2}\sin^2\theta[3\cos(2\phi)\cos(nt) + 4\sin(2\phi)\sin(nt)], \quad (5)$$

166 where  $(r, \theta, \phi, t)$  are the time-dependent spherical polar coordinates ( $\theta$  given as co-latitude),  
 167 which will rotate compared to stationary reference frame but are fixed with regard to  
 168 Europa itself,  $\epsilon$  is the Europen orbital eccentricity, and  $Z$  is a constant given by

$$Z = \frac{3Gm^*R_s^2}{2a^{*3}} \quad (6)$$

169 where  $G$  is the gravitational constant,  $m^*$  is the mass of Jupiter,  $R_s$  is the radius of Eu-  
 170 ropa and  $a^*$  is the semi-major axis of the Europen orbit.

171 In order to derive surface stresses from the gravitational potential, the model pre-  
 172 sumes a four-layered Maxwell solid structure for Europa, as described by Jaeger et al.  
 173 (2009). This structure includes a silicate core, an oceanic layer of liquid water, and an  
 174 ice crust. The ice crust is further divided into an inner, warm, viscoelastic, and ductile  
 175 layer surrounded by an outer, cold, brittle layer. The model calculates the stress ten-  
 176 sor,  $\tau$ , although due to context there are no stresses in the  $r$  direction, leaving only  $\tau_{\theta\theta}$ ,  
 177  $\tau_{\phi\phi}$ , and  $\tau_{\theta\phi} = \tau_{\phi\theta}$ . This is shown as follows, where a tilde denotes a complex quan-  
 178 tity:

$$\begin{aligned} \tau_{\theta\theta} = \frac{Z}{2gR_s} Re & \left[ \left( \tilde{\beta}_1(2b) - \tilde{\gamma}_1(2b)\cos(2\theta) \right) e^{i(2\phi+2bt)} \right. \\ & + 3\epsilon \left( \tilde{\beta}_1(n) - \tilde{\gamma}_1(n)\cos(2\theta) \right) e^{int}\cos(2\phi) \\ & - \epsilon \left( \tilde{\beta}_1(n) + 3\tilde{\gamma}_1(n)\cos(2\theta) \right) e^{int} \\ & \left. - 4\epsilon \left( \tilde{\beta}_1(n) - \tilde{\gamma}_1(n)\cos(2\theta) \right) ie^{int}\sin(2\phi) \right], \end{aligned} \quad (7)$$

$$\begin{aligned} \tau_{\phi\phi} = \frac{Z}{2gR_s} Re & \left[ \left( \tilde{\beta}_2(2b) - \tilde{\gamma}_2(2b)\cos(2\theta) \right) e^{i(2\phi+2bt)} \right. \\ & + 3\epsilon \left( \tilde{\beta}_2(n) - \tilde{\gamma}_2(n)\cos(2\theta) \right) e^{int}\cos(2\phi) \\ & - \epsilon \left( \tilde{\beta}_2(n) + 3\tilde{\gamma}_2(n)\cos(2\theta) \right) e^{int} \\ & \left. - 4\epsilon \left( \tilde{\beta}_2(n) - \tilde{\gamma}_2(n)\cos(2\theta) \right) ie^{int}\sin(2\phi) \right], \end{aligned} \quad (8)$$

$$\begin{aligned} \tau_{\phi\theta} = \tau_{\theta\phi} = \frac{2Z}{gR_s} Re & \left[ \tilde{\Gamma}(2b)ie^{i(2\phi+2bt)}\cos\theta \right. \\ & - 4\epsilon\tilde{\Gamma}(n)ie^{int}\cos\theta\cos(2\phi) \\ & \left. - 3\epsilon\tilde{\Gamma}(n)e^{int}\cos\theta\sin(2\phi) \right] \end{aligned} \quad (9)$$

<sup>179</sup> where

$$\tilde{\beta}_1 = \tilde{\mu} \left[ \tilde{\alpha}(\tilde{h} + 3\tilde{l}) \right] \quad (10)$$

$$\tilde{\gamma}_1 = \tilde{\mu} \left[ \tilde{\alpha}(\tilde{h} - \tilde{l}) \right] \quad (11)$$

$$\tilde{\beta}_2 = \tilde{\mu} \left[ \tilde{\alpha}(\tilde{h} - 3\tilde{l}) \right] \quad (12)$$

$$\tilde{\gamma}_2 = \tilde{\mu} \left[ \tilde{\alpha}(\tilde{h} + \tilde{l}) \right] \quad (13)$$

$$\tilde{\alpha} = \frac{3\tilde{\lambda} + 2\tilde{\mu}}{\tilde{\lambda} + 2\tilde{\mu}} \quad (14)$$

$$\tilde{\Gamma} = \tilde{\mu}\tilde{l} \quad (15)$$

<sup>180</sup> where  $\tilde{h}$  and  $\tilde{l}$  are the complex Love numbers (discussed further in Section 3.1), and  $\tilde{\lambda}$   
<sup>181</sup> and  $\tilde{\mu}$  are the complex Lamé parameters given by

$$\tilde{\mu}(\omega) = \mu \left( \frac{1}{1 - i\Delta} \right) \quad (16)$$

$$\tilde{\lambda}(\omega) = \lambda \left( \frac{1 - i\Delta \left( \frac{2\mu+3\lambda}{3\lambda} \right)}{1 - i\Delta} \right) \quad (17)$$

where  $\omega$  is the rotation rate of the tidal effect,  $\Delta = \frac{\mu}{\eta\omega}$ , and  $\eta$  is the viscosity. See Walding et al. (2024) for validation against Wahr et al. (2009). The resulting stress field is shown in Fig. 1.

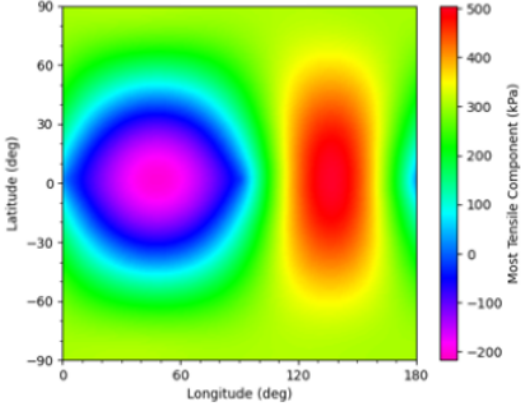


Figure 1: The calculated stress field across the Europa surface. The heatmap is only given up to 180° East as the stress field is symmetric across the Eastern and Western hemispheres.

These equations only pertain to surface stresses however, while the present implementation requires stresses at depth. These subsurface stresses are determined by a simple heuristic relation;

$$\sigma(r, \theta, \phi) = \left( \frac{r}{R_E} \right)^2 \cdot \sigma(\theta, \phi) \quad (18)$$

where  $R_E$  is the radius of Europa.

## 2.2 Deformation and Fracture Growth

The modelling procedure consists of numerically solving mechanical deformation partial differential equations on a discretised domain representing the Europa ice crust, where the domain is assumed to be homogeneous (aside from inserted features), isotropic and linear elastic. The three-dimensional geometry is meshed automatically and the deformation and damage to the domain is computed across the surface, before inserting mechanically active fractures. Each fracture then becomes part of the domain and influences the stress field in its vicinity. Meshes are composed of isoparametric quadratic triangles and tetrahedra. Around fracture tips, isoparametric quadratic quarter-point triangles and tetrahedra are inserted to reduce numerical errors in the displacement field. At each step, stress intensity factors are computed ahead of each fracture tip location to control changes to the fracture geometry. As growth progresses, the geometry evolves and the domain is progressively remeshed to capture changes due to the fractures' evolution. This operation is described in Algorithm 1.

**Algorithm 1** Deformation of the domain and fracture growth

---

```

while Current growth step < Maximum growth steps & State of model has changed do
    Define initial state
    Discretise domain (create mesh)
    Map variables (displacement and damage)
    Apply boundary conditions and stresses
    Compute deformation
    for each fracture do
        for each fracture tip do
            Compute propagation criterion (Equation 20)
            if Propagation criterion fulfilled then
                Compute extension criterion (Equations 21 and 22)
                Compute angle criterion (Equation 23)
                Compute new tip location
            end if
            Resolve intersections
            Update fracture geometry
        end for
    end for
end while

```

---

203    **2.2.1 Mechanical Deformation**

204    A three-dimensional volumetric finite element method is used to solve for the me-  
 205    chanical deformation of the system, computed as elastic deformation (Cook et al., 2007),  
 206    in response to the tidal stresses, and thus determining the distribution of the displace-  
 207    ment, stress and strain fields across the ice crust. This assumes that the outer layer of  
 208    ice is in a brittle and linear elastic state, which given the very low temperatures of the  
 209    European surface (110 K in the warmest equatorial region, down to 50 K in the polar vicin-  
 210    ity (Ashkenazy, 2019)) is a reasonable assumption.

211    **2.2.2 Fracture Growth**

212    Fracture growth assumes a quasi-static regime and is modelled using Stress Inten-  
 213    sity Factors (SIFs). The opening deformation ( $K_I$ ), in-plane deformation ( $K_{II}$ ) and out-  
 214    of-plane deformation ( $K_{III}$ ) SIFs are calculated for every fracture's tips using the dis-  
 215    placement correlation method described by Nejati et al. (2015). The SIFs then deter-  
 216    mine whether a given fracture tip will extend, and the magnitude of extension, by means  
 217    of growth criteria (Paluszny & Zimmerman, 2013).

218    The mixed-mode propagation criterion developed by Richard et al. (2014) is used  
 219    to determine whether or not a fracture tip will extend. The evaluated SIFs at a fracture  
 220    tip are used to compute a derived quantity  $K_V$ , as follows;

$$K_V = \frac{1}{2}K_I + \frac{1}{2}\sqrt{{K_I}^2 + 4(\alpha_1 K_{II})^2 + 4(\alpha_2 K_{III})^2} \quad (19)$$

221    where  $\alpha_1$  is the ratio of mode I (opening) fracture toughness to mode II (in-plane shear),  
 222    and  $\alpha_2$  the same ratio for mode III (out-of-plane shear); both empirical parameters of  
 223    value  $1.3268^{-1}$  and  $0.6297^{-1}$  respectively.  $K_V$  is then compared to the critical stress in-  
 224    tensity factor,  $K_{IC}$ ,

$$K_V \geq K_{IC} \quad (20)$$

For fracture tips where this criterion is fulfilled, the extension magnitude and orientation are then determined by further criteria, drawn from Richard et al. (2005) and Thomas et al. (2020).

The extension criterion given by Thomas et al. (2020) is a two-step Paris-type (Paris & Erdogan, 1963) law governed by the strain energy release rate at each fracture tip,  $\mathcal{G}$ , calculated with an  $I$ -integral detailed in Nejati et al. (2015). The criterion is controlled by three parameters:  $\Delta a_v$ ,  $\beta_f$  and  $\beta_n$ , where the  $\beta$  parameters, or Paris Exponents, are empirical quantities given in Table 1 and  $\Delta a_v$  is the original radius of a given fracture. The first step of the equation is as follows:

$$\Delta a_f = \Delta a_v \left( \frac{\mathcal{G}_f}{\mathcal{G}_v} \right)^{\beta_f} \quad (21)$$

where  $\Delta a_f$  indicates the maximum allowable extension for any tip within a fracture.  $\mathcal{G}_f$  represents the peak value of the energy release rate  $\mathcal{G}$  observed at any fracture tip, while  $\mathcal{G}_v$  denotes the maximum energy release rate throughout the entire volume of the material. The extension for a specific fracture tip, denoted as  $\Delta a_n$ , is calculated based on these values, reflecting the localised response of the material at that particular tip, given as

$$\Delta a_n = \Delta a_f \left( \frac{\mathcal{G}_n}{\mathcal{G}_f} \right)^{\beta_n} \quad (22)$$

where  $\mathcal{G}_n$  is  $\mathcal{G}$  at the tip. Each tip that passes the propagation criterion will then extend by  $\Delta a_n$ .

The criterion for propagation angle is adapted from Richard et al. (2005), which therein calculates two angles - perpendicular and tangential to the fracture front. In the ICGT the tangent angle is excluded from consideration in service of model simplicity. The perpendicular, or deflection, angle  $\varphi$  is calculated as follows;

$$\varphi = \mp \left[ A \frac{|K_{II}|}{K_I + |K_{II}| + |K_{III}|} + B \left( \frac{|K_{II}|}{K_I + |K_{II}| + |K_{III}|} \right)^2 \right] \quad (23)$$

where  $A = 140^\circ$  and  $B = -70^\circ$ . Further details on this methodology can be found in Paluszny and Zimmerman (2013) and Thomas et al. (2020).

### 2.3 Quantification

The quantification strategy for this work is a single probe approach. Given a homogeneous domain, a probe fracture consisting of a planar disc with twenty fracture tips is inserted into the domain at various locations. Each fracture has a radius of 1 km and is inserted at a depth of 1.5 km. The simulation then progresses for two growth steps. This is to allow the stress fields and geometry to settle around the probe fracture (this will not be a steady state, however, as fractures at this stage in almost all configurations will continue to grow). The following parameters are then extracted:  $K_I$ ,  $K_{II}$ ,  $K_{III}$ , and the growth vector for the next step. The derived quantity  $K_V$  is then calculated with Eqn. 19.

The growth vectors of all of the tips in a fracture are examined collectively to determine the tip that is to most extend in the next step, and the tip to extend the least. The fracture tips' locations are used to calculate the centroid of the fracture, and then the vectors from the centroid to the most and least extending tips are calculated. The

normal of these two vectors is taken, which is then used to calculate with simple trigonometry the in-plane and out-of-plane deflection,  $\phi_{frac}$  and  $\psi_{frac}$  respectively, of the fracture body. The arbitrary reference plane is taken as the  $x$ - $y$  plane, and the reference direction is the  $x$ -axis. This thus yields the five tip-based parameters and four fracture-based parameters used for quantification in this work. This process is also applied to the growth vector of greatest extension to calculate  $\phi$  and  $\psi$  for the direction of greatest extension.

In the case with a subsurface meltwater lens, the probe location is varied to quantify the impact of the lens as its presence significantly affects the spatial dependence of the fields. The number and layout of probe locations differs depending on the simulation purpose. In general, each simulation considers a single fracture probe which changes location over the structure of a grid, in order to capture for individual fractures how the meltwater lens affects their growth. Growth is quantified independently from fracture interaction which would incorporate further complexity due to the overlapping of stress concentration regions. The result is a distribution of growth behaviour quantified over a grid on the  $x$ - $y$  plane overlying the lens, parallel to the surface.

Simulations consider three initial orientations of the fracture probe, namely horizontal, vertical and diagonal (Fig. 2), with normal vectors  $(0, 0, 1)$ ,  $(1, 0, 0)$  and  $(1, 1, 1)$  respectively. These investigate the effect of initial conditions on the evolution of fracture geometry, as well as the effect on stress concentrations.

### 3 Simulation Setup

#### 3.1 Physical Parameters and Love Numbers

The physical quantities that parameterize the system along with their taken values are detailed in Table 1. The Love numbers  $h$ ,  $k$ , and  $l$  are dimensionless, complex parameters that describe how a body responds to tidal forces. The Love number  $k$  is not employed in this work. The overall model incorporates effects from layers not directly simulated, such as the silicate core, through their influence on these Love numbers. The Love numbers as used in this work are given in Table 2. For further detail on the selection and use of the physical parameters and Love numbers in this work, see Walding et al. (2024).

#### 3.2 Geometry of the Domain

The geometry used in this work is cuboidal, of dimension  $200 \text{ km} \times 200 \text{ km} \times 20 \text{ km}$ , although only the interior  $100 \text{ km} \times 100 \text{ km}$  is available for fracture placement. This is such that the lens and the domain boundary do not interact and create edge effects. The  $20 \text{ km}$  side is in the core-ward  $z$ -direction and the top of the slab is taken to be the surface of Europa. At this length scale, the surface of Europa can be approximated to be flat. These domains are shown in context in Fig. 3.

There still exists uncertainty and debate as to the thickness of the solid ice layer, but there is some agreement on overall water layer thickness (both oceanic and ice) at close to  $120 \text{ km}$  (Billings & Kattenhorn, 2005; McKinnon, 2004). The oceanic layer is then estimated to be  $100 \text{ km}$  thick (Pappalardo et al., 1999), thus leaving  $20 \text{ km}$  for the total ice layer (Lucchitta & Soderblom, 1982; Schenk, 2002; Turtle & Ivanov, 2002) (McKinnon, 1999; Ojakangas & Stevenson, 1989a). This therefore is the value taken for the  $20 \text{ km}$  core-ward side length of the domain.

A Dirichlet boundary condition fixes the bottom of the domain (defined as the inner face toward the core), the outer surface (the top) is a free surface, with the other faces having symmetric boundary conditions. Stresses are applied as triaxial loads, although in the present work there is never a non-zero stress component in the  $z$ -direction. Load

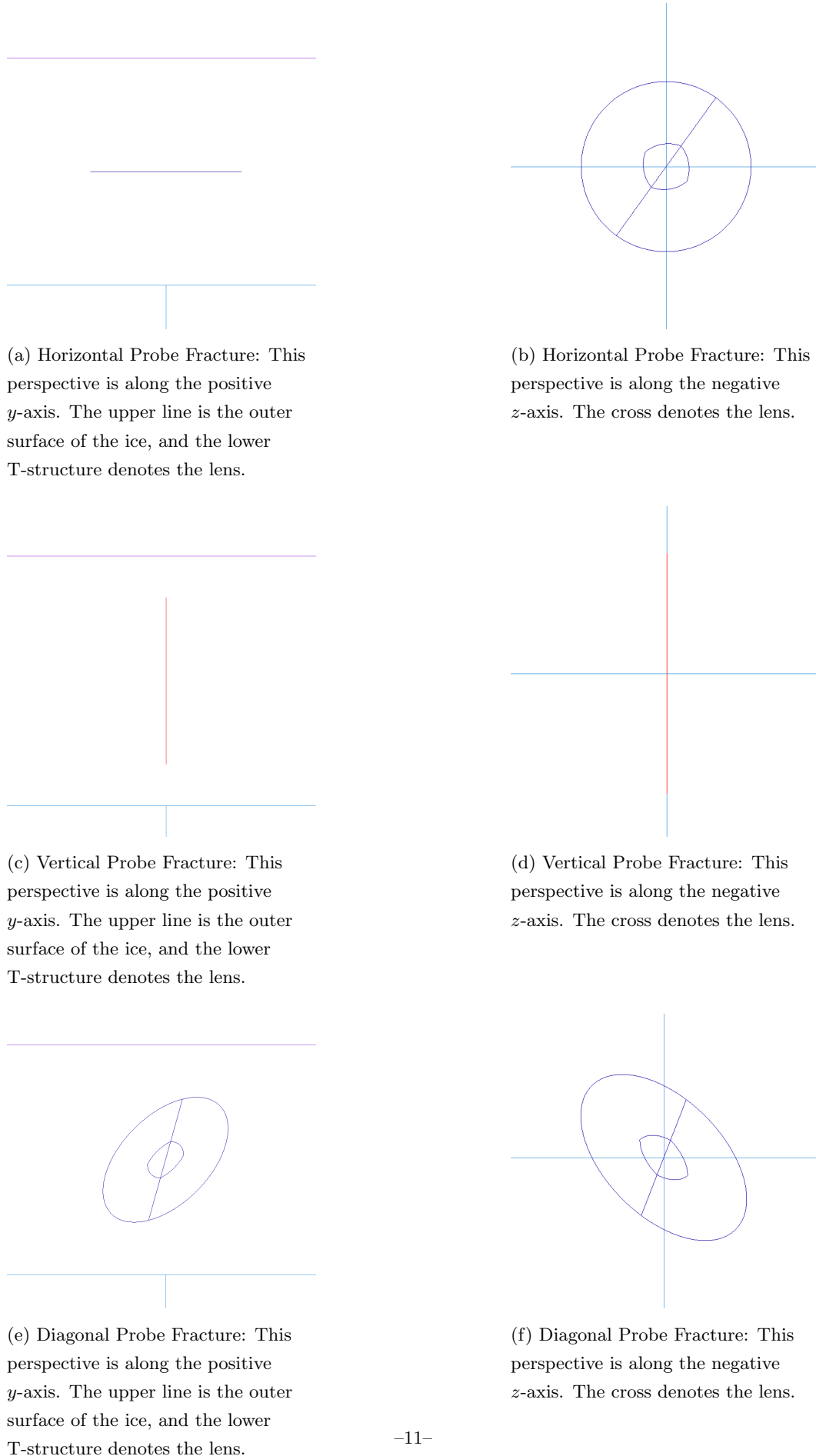


Figure 2: Schematic representations of probe fractures. The fractures are the central elements.

Table 1: Summary of physical parameters.

Physical Parameter	Symbol	Value	Unit	Reference
Young's Modulus of Ice	$E$	9	GPa	(Nimmo, 2004)
Fracture Toughness of Ice	$K_{IC}$	108	$\text{kPa} \cdot \text{m}^{\frac{1}{2}}$	(Goodman, 1980)
Poisson's Ratio of Ice	$\sigma$	0.33	-	(Sinha, 1989)
Tensile Strength of Ice	$UTS$	2	MPa	(Petrovic, 2003)
Diurnal Angular Rate	$f_{Diurnal}$	$2.0485 \times 10^{-5}$	$\text{rad} \cdot \text{s}^{-1}$	(Burns et al., 1986)
NSR Angular Rate	$f_{NSR}$	$1.7434 \times 10^{-14}$	$\text{rad} \cdot \text{s}^{-1}$	(Geissler et al., 1998)
Orbital Eccentricity	$\epsilon$	0.0094	-	(Cassen et al., 1979)
Jovian Mass	$M_{Jupiter}$	$1.898 \times 10^{27}$	kg	(Jacobson et al., 2000)
Europan Mass	$M_{Europa}$	$4.799 \times 10^{22}$	kg	(Jacobson et al., 2000)
Europan Radius	$R_{Europa}$	$1.561 \times 10^3$	km	(Archinal et al., 2018)
Jovian Semi-Major Axis	$a_{Jupiter}$	$7.78479 \times 10^8$	km	(Office et al., 2016)
Europan Semi-Major Axis	$a_{Europa}$	$6.71 \times 10^5$	km	(Cassen et al., 1979)
Europan Surface Gravity	$g$	1.315	$\text{m} \cdot \text{s}^{-2}$	<i>derived</i>
Lamé $\mu$	$\mu$	3.487	GPa	(Gammon et al., 1983)
Lamé $\kappa$	$\kappa$	9.3	GPa	(Gammon et al., 1983)
Brittle Ice Viscosity	$\nu_{Brittle}$	$1 \times 10^{22}$	$\text{Pa} \cdot \text{s}$	(Wahr et al., 2009)
Paris Exponent $f$	$\beta_f$	0.35	-	(Paris & Erdogan, 1963)
Paris Exponent $n$	$\beta_n$	1	-	(Paris & Erdogan, 1963)

Table 2: Model Love numbers, drawn from Wahr et al. (2009).

Love Number	Symbol	Real Component	Imaginary Component
Diurnal Love Number $h$	$h_{Diurnal}$	1.192	$-6.293 \times 10^{-5}$
NSR Love Number $h$	$h_{NSR}$	1.813	$-4.186 \times 10^{-3}$
Diurnal Love Number $l$	$l_{Diurnal}$	0.3094	$-2.903 \times 10^{-5}$
NSR Love Number $l$	$l_{NSR}$	0.4748	$-2.766 \times 10^{-3}$

stresses are calculated by the tidal stress model at each mesh node within the domain, and are applied as *in situ* stresses at each location.

### 3.2.1 Melt Water Lenses

Melt water lenses are included in simulations as directly modelled heterogeneities within the ice. Taking the example of the *Thera Macula*, a region of chaos terrain approximately 80 km in diameter, used in Schmidt et al. (2011) as representative of this phenomenon, the lenses are modelled with a volume of 20,000 km<sup>3</sup> and at a depth of 3 km, which is also supported by recent research by Vilella et al. (2020). The heterogeneities are geometrically represented as spherical caps of height one twentieth of the radius of the source sphere, yielding lenses of height 6.87 km and flat-face radius of 42.9 km (and therefore diameter 85.8 km, close correspondence to the *Thera Macula*). Finally, the bounding circle constraining the cap is chamfered to yield a softer edge as shown in Fig. 4. This is to prevent unnatural stress concentration at the edge due to precise geometry. As the lens is a melt water pocket, the lens is modelled as being soft yet unable to be fractured.

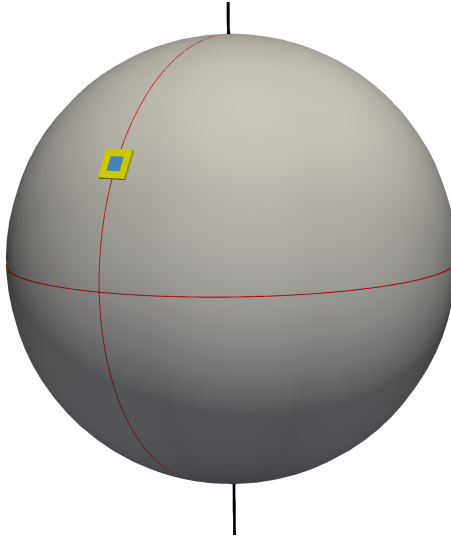


Figure 3: The surface ice of Europa is shown in light gray with a radius of 1561 km, with the equator and subjovian meridian in red, and the rotation axis in black. An example slab domain of dimension 200 km  $\times$  200 km  $\times$  20 km centred at 30°N 0° is shown in yellow, with the interior 100 km  $\times$  100 km active simulation region in blue.

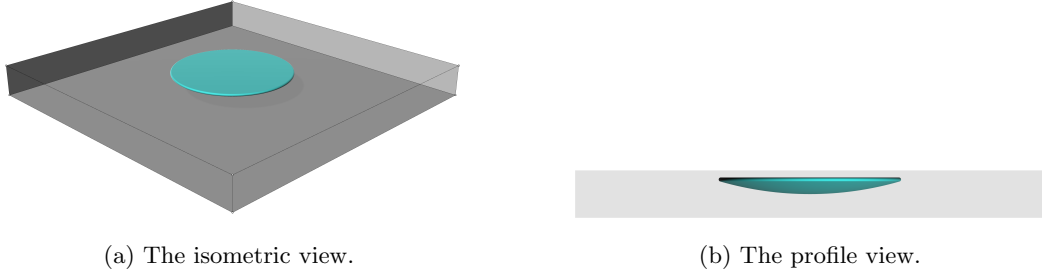


Figure 4: The lens geometry for the slab domain.

## 4 Results

The visualisation heatmaps presented in this section are the individual fracture probe results in the same domain interpolated with the Python Scipy library's `griddata` function, to create the gradients and contours. Each individual probe simulation models the ice crust with a discretised domain comprised of approximately 43,000 nodes and 35,000 elements. Each heatmap evaluates a potential scenario of fracture growth, given a set of initial geometric conditions for the fractures and a set of external boundary conditions, depending on the longitude of the lens.

The results presented in Fig. 5 pertain to simulations run in a homogeneous domain without a lens, to act as a base case for comparison with the lens cases. In Fig. 5a, showing a heatmap for  $K_V$  with vertical probe fractures, there is a smooth transition from West to East of low stress to high stress, whereas the heatmap of the same with horizontal probe fractures (Fig. 5b) still shows a very weak West-East trend though with distinct irregularities that are not present in the vertical case. The quiver plot for  $\phi$  (the deflection within the  $x$ - $y$  plane away from the line  $x = 0$ ) with vertical probe fractures

339 presented in Fig. 5c shows total uniformity with no deflection. By contrast the  $\phi$  quiver  
 340 plot for horizontal probes in Fig. 5d shows no ordered structure with completely arbit-  
 341 rary directionality.

342 The following results are drawn from quantification runs executed in the vicinity  
 343 of a subsurface meltwater lens, designed to study the effect that the lens has on the spa-  
 344 tial distribution of stresses and propagation angles, as well as how these parameters change  
 345 with regard to the longitude of the test domain. The fractures are distributed in a 13  
 346 by 13 grid across the domain, with a simulation for each of the three orientations run  
 347 at each grid location, and the domain run at 0°E, 60°E and 120°E, for a total of 1,521  
 348 simulations.

349 The first set of results in Fig. 6 are heatmaps of the respective parameters at 30°N  
 350 0°E with diagonal test fractures. Figs. 6a and 6b for  $K_I$  and  $K_{II}$  show strong spatial  
 351 dependence, with  $K_I$  having a stress concentration in the South-West quarter peaking  
 352 at around  $30 \text{ MPa} \cdot \text{m}^{\frac{1}{2}}$ , and  $K_{II}$  with a mirror concentration in the North-East quar-  
 353 ter at a lower around  $20 \text{ MPa} \cdot \text{m}^{\frac{1}{2}}$ . This is contrasted against the largely symmetric ring  
 354 formation exhibited by the  $K_{III}$  heatmap, seen in Fig. 6c, peaking at around  $10 \text{ MPa}$   
 355  $\cdot \text{m}^{\frac{1}{2}}$ . The combination of the three SIFs, where  $K_I$  and  $K_{II}$  have opposite formations  
 356 and  $K_{III}$  is symmetric, leads to a largely symmetric  $K_V$  (Fig. 6d) of maximum magni-  
 357 tude around  $35 \text{ MPa} \cdot \text{m}^{\frac{1}{2}}$ .

358 Figs. 7 and 8 are quiver plots of both extension direction and fracture body ori-  
 359 entation. Fig. 7a shows on the whole expected behaviour, as the probe fractures in this  
 360 case were diagonally oriented and this is largely maintained, though there is some irreg-  
 361 ularity in the upper right region, in close correspondence to the region where  $K_{II}$  is high-  
 362 est. In Fig. 7b it can be seen that the out-of-plane deflection leads to a bistable config-  
 363 uration, where a fracture will settle into a 30° tilt in either direction. Curvature is seen  
 364 in the interior lens region of Fig. 8a, where the fractures are growing perpendicularly to  
 365 the edge of the lens. This excludes a diagonal region from the top left to the bottom right,  
 366 bisecting the lens. The overall growth on different sides of this divide are in different di-  
 367 rections. Of more interest in this case however, is Fig. 8b, where it can be seen that the  
 368 vertical deflection of fractures across the tested domain is very limited.

369 Fig. 9 shows  $K_I$  heatmaps with all three probe fracture orientations and at differ-  
 370 ent longitudes (0°E, 60°E and 120°E). The colourbar is normalised across all five sub-  
 371 figures. The results from the horizontal and vertical orientations are largely similar in  
 372 form, with stress concentration in a ring following the edge of the lens, though the ver-  
 373 tical probe fracture exhibits heightened stresses in the bottom half. The diagonal and  
 374 combined orientations however are quite divergent, with the diagonal probe fracture show-  
 375 ing a large stress increase in the lower left quadrant. These figures together show that  
 376 the initial condition of the fracture is quite influential on the stress conditions, which is  
 377 expected in the earliest stages of a simulation. Significant change is observed by longi-  
 378 tude, with the heatmap at 60°E showing only very weak stress concentration following  
 379 the edge of the lens, and the heatmap at 120°E being the opposite of that seen at 0°E,  
 380 with the heightened stresses now in the upper right. This longitudinal variation is ob-  
 381 served across all measured parameters to some degree, as seen in the following.

382 The maximum, minimum and average values of each parameter by longitude are  
 383 shown in Figs. 10 and 11. There were simulations run for every 5° of longitude, where  
 384 at each longitude the fractures were in a 7 by 7 grid across the domain, and each loca-  
 385 tion was run with each of the three orientations for a total of 5,439 simulations. The light  
 386 grey lines show a randomly selected quarter of the individual simulations where possi-  
 387 ble.

388 The results presented in Figs. 12 and 13 are of different form, and are qualitative  
 389 views of dense fracture networks to show visually how the fractures grow. The network

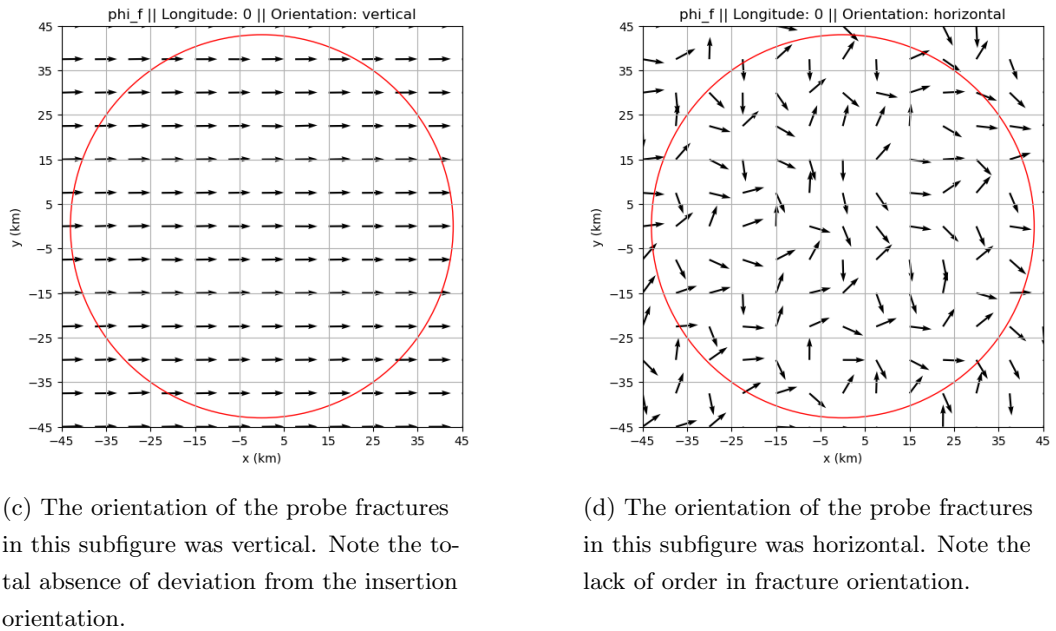
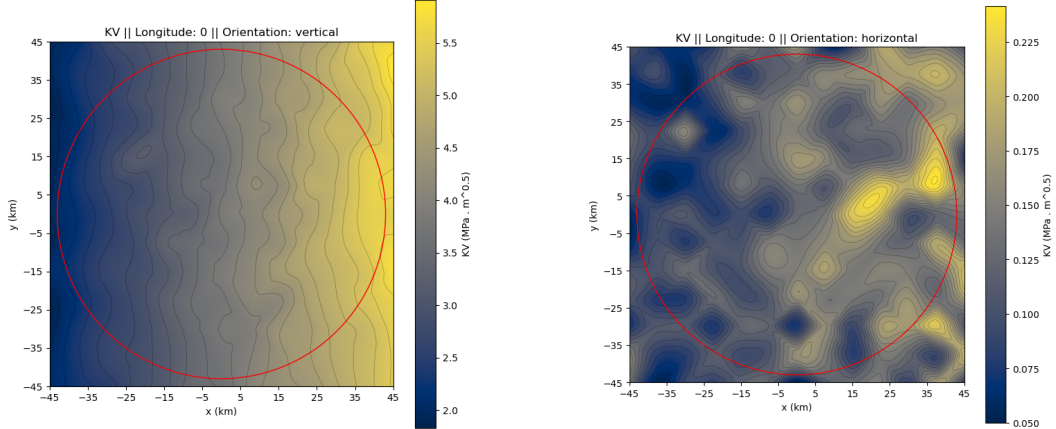
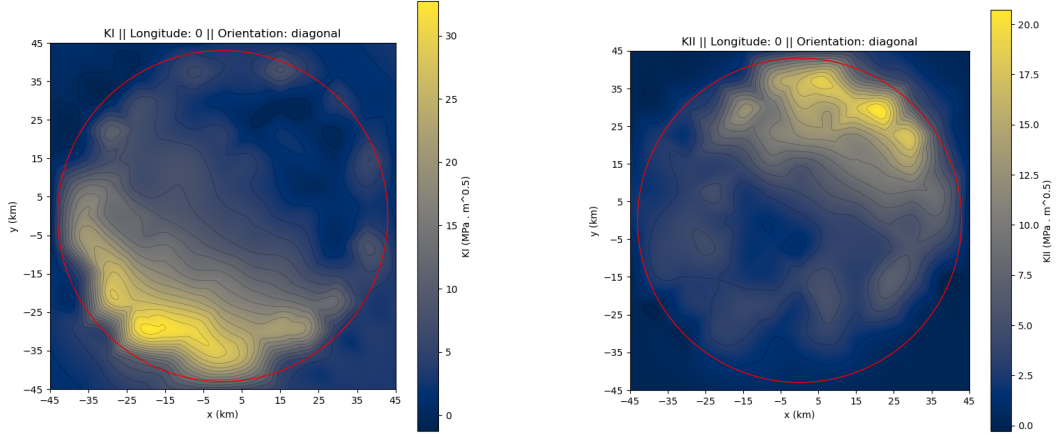
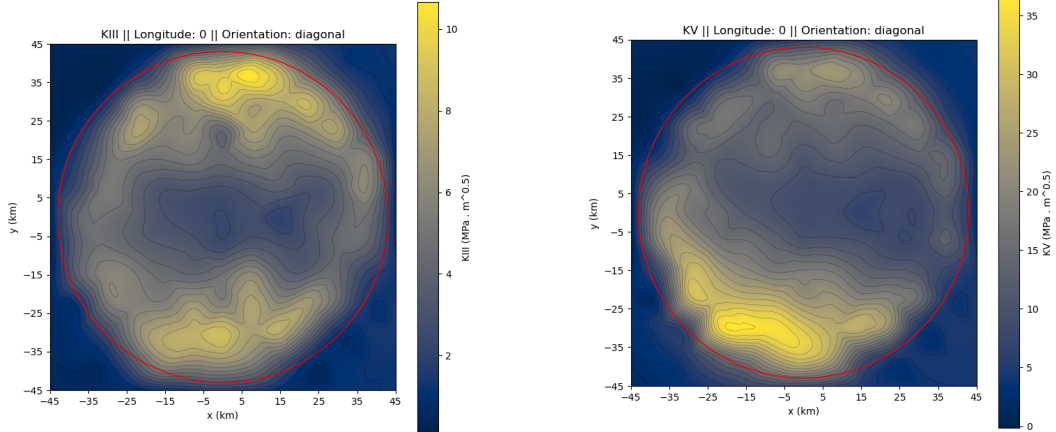


Figure 5: Homogeneous domain, no lenses. The red circles denote where the subsurface meltwater lens would be were it present for comparison with the later simulations. Subfigures (a) and (b) give the values of  $K_V$  across a slab that does not contain a subsurface lens. Subfigures (c) and (d) give the values of  $\phi$  for fracture bodies (the deflection within the  $x$ - $y$  plane away from the line  $x = 0$ ) across a slab that does not contain a subsurface lens, where the lines are the normals to the plane formed from the most and least extending fracture tips' vectors from the fracture centroid. Location: 30°N 0°E.



(a)  $K_I$ : Note the large asymmetry of the stress field.

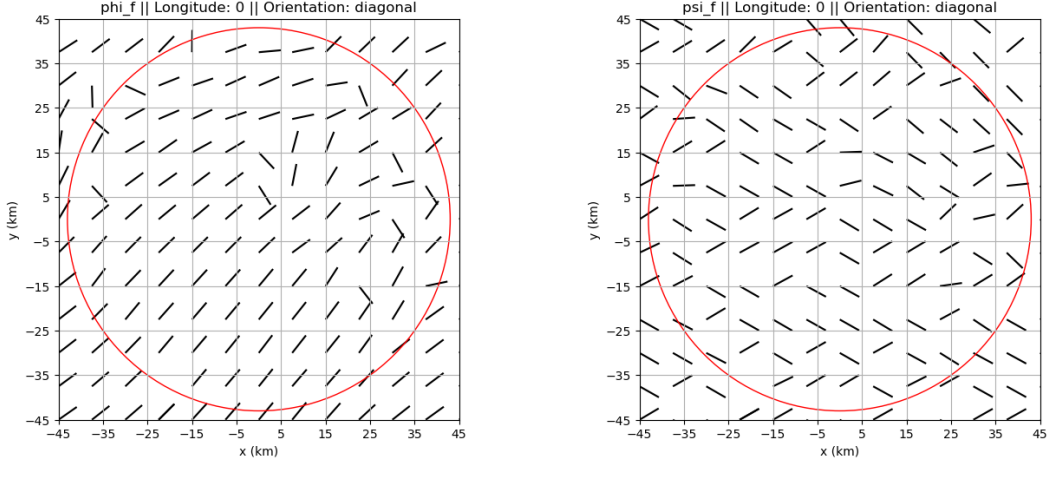
(b)  $K_{II}$ : Note again the similarly large asymmetry of the stress field as compared to  $K_I$ , though opposite and also slightly lesser in magnitude.



(c)  $K_{III}$ : In this case the stress field is symmetric about the line  $y = 0$ , though of substantially smaller magnitude than for  $K_I$  and  $K_{II}$ .

(d)  $K_V$ : The distribution is a combination of that of  $K_I$ ,  $K_{II}$  and  $K_{III}$ , though with the peak seen in the  $K_I$  distribution dominating.

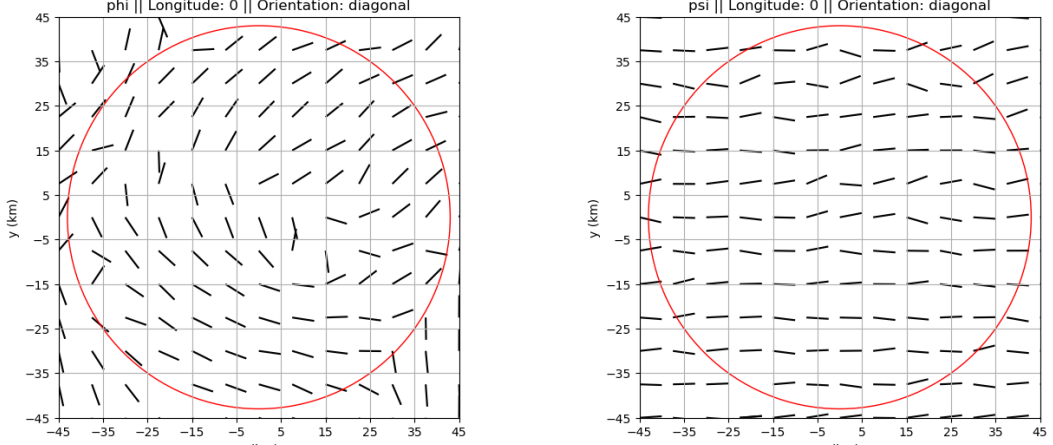
Figure 6: The values of modal SIFs presented across a domain that contains a subsurface lens, the edge of which is denoted by the red line. The orientation of the probe fractures was diagonal. Each subfigure has 507 constituent simulations. Location: 30°N 0°E.



(a)  $\phi$ : The deflection within the  $x$ - $y$  plane away from the line  $x = 0$ .

(b)  $\psi$ : The deflection away from the  $x$ - $y$  plane.

Figure 7: The values of  $\phi$  and  $\psi$  for fracture bodies across a slab that contains a sub-surface lens, the edge of which is denoted by the red line. The orientation of the probe fractures was diagonal. The lines are the normals to the plane formed from the most and least extending fracture tips' vectors from the fracture centroid. Each subfigure has 507 constituent simulations. Location: 30°N 0°E.



(a)  $\phi$ : The deflection within the  $x$ - $y$  plane away from the line  $x = 0$ .

(b)  $\psi$ : The deflection away from the  $x$ - $y$  plane.

Figure 8: The values of  $\phi$  and  $\psi$  for fracture extension across a slab that contains a sub-surface lens, the edge of which is denoted by the red line. The orientation of the probe fractures was diagonal. The lines are the normals to the plane formed from the most and least extending fracture tips' vectors. Each subfigure has 507 constituent simulations. Location: 30°N 0°E.

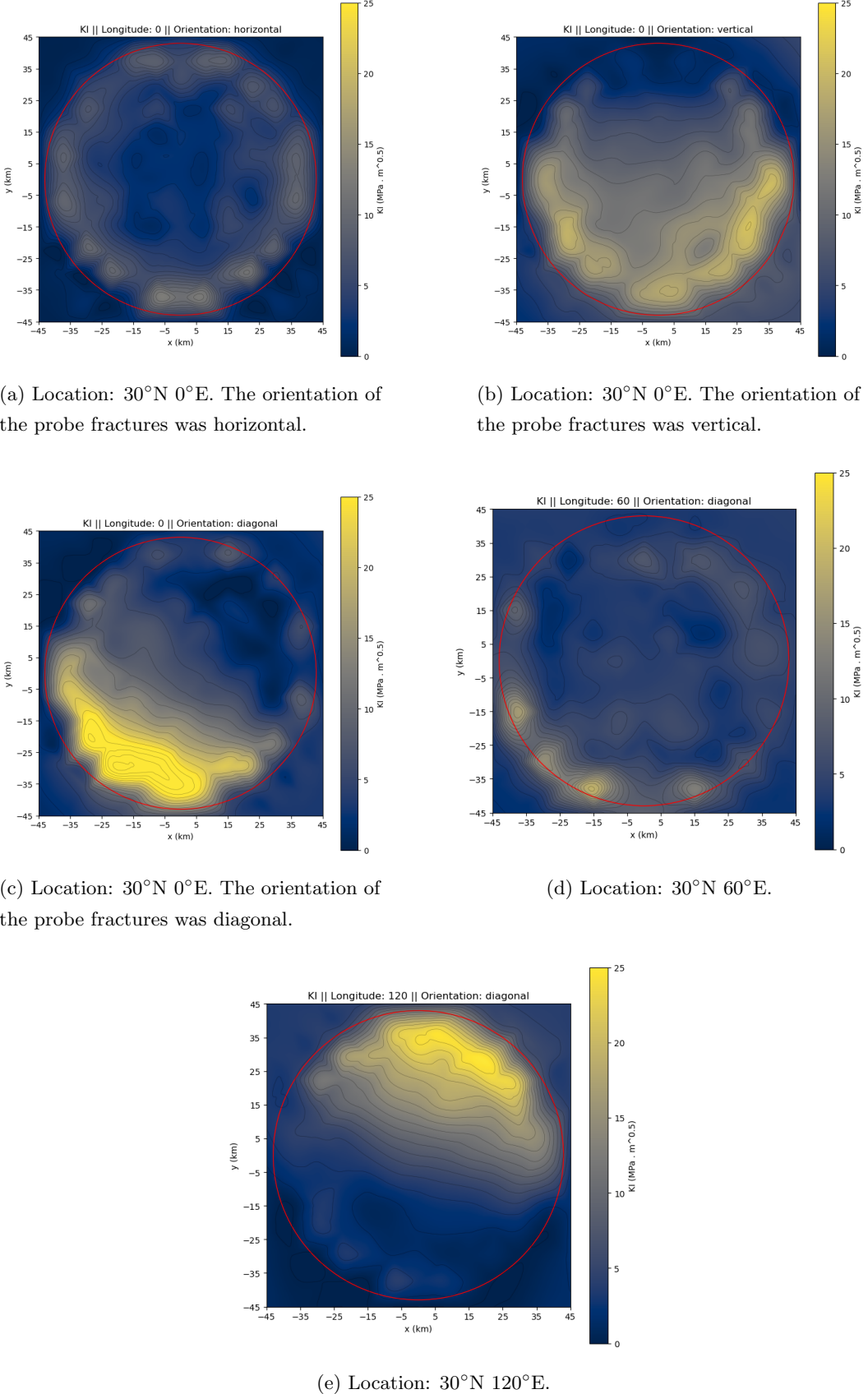
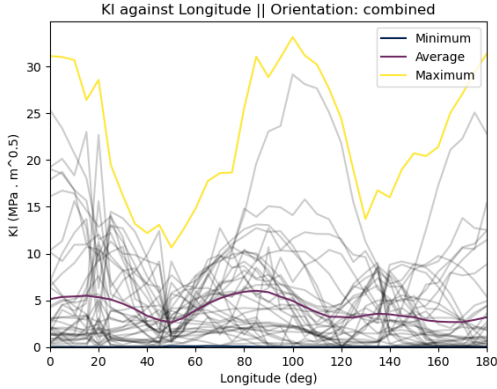
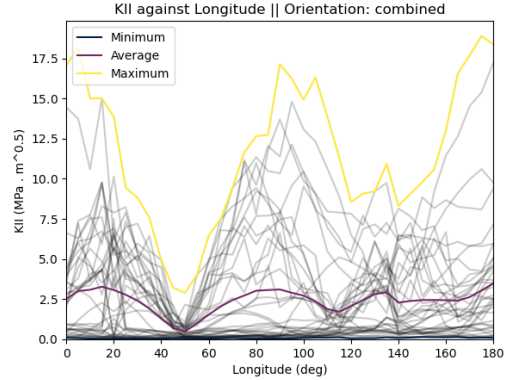


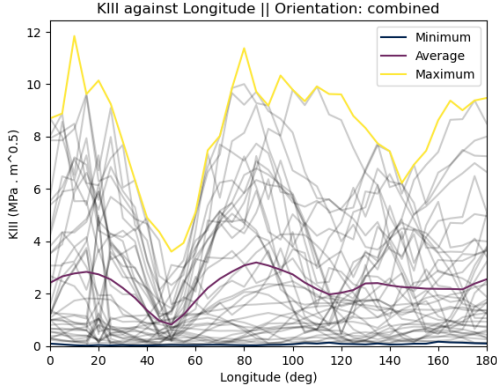
Figure 9: The values of  $K_I$  across slabs that contains a subsurface lens, the edge of which is denoted by the red line. Subfigures (a), (b) and (c) show different probe fracture orientations. (c), (d) and (e) show different locations. Each subfigure has 507 constituent simulations.



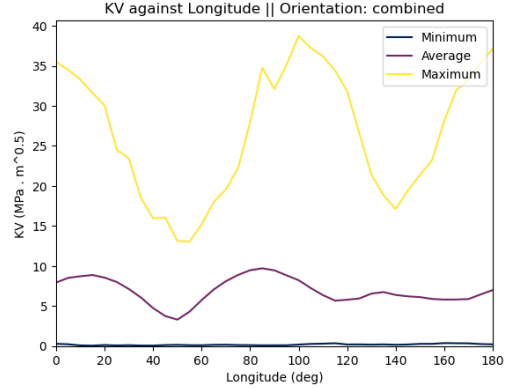
(a)  $K_I$ : There are distinct sharp peaks in the maximum line around  $0^\circ$  and  $100^\circ$ . In the average line there are smooth peaks between  $0^\circ$  and  $120^\circ$ , with a close to monotonically decreasing line beyond.



(b)  $K_{II}$ : There are peaks in the same areas as with Fig. 10a for the maximum line, though the valley at  $50^\circ$  is deeper and sharper, with this mirrored in the average line.

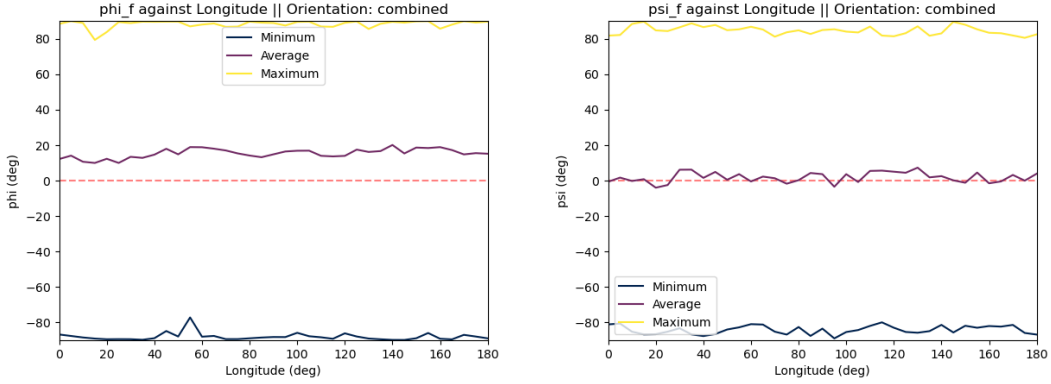


(c)  $K_{III}$ : The average line follows the same trend as with  $K_I$  and  $K_{II}$ , though the maximum line has a significantly less pronounced valley around  $140^\circ$ .



(d)  $K_V$ : The maximum line has smooth and close to symmetric peaks around  $0^\circ$  and  $100^\circ$ , similar to  $K_I$ . The average line again shows smooth peaks, though they are closer together at  $20^\circ$  and  $80^\circ$ , and the region after the second peak is flat.

Figure 10: The measured  $K$  parameters as a function of longitude, giving their respective maximum, minimum and average values. The light grey lines, where present, show a random quarter of the simulation runs used to calculate those values. The difference between the first half of the average lines and the second half corresponds to the difference in form between the stress concentrations in Fig. 1. These figures are the result of 5,439 simulations.



(a)  $\phi$ : The deflection within the  $x$ - $y$  plane away from the line  $x = 0$ . The maximum and minimum lines are in the vicinity of  $90^\circ$ , though the average line is consistently around  $10^\circ$  to  $20^\circ$ .

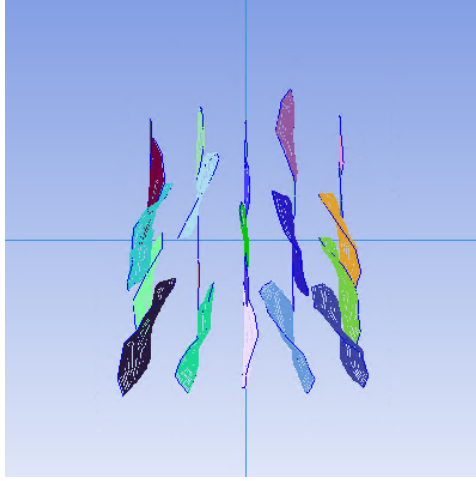
(b)  $\psi$ : The deflection away from the  $x$ - $y$  plane. The maximum and minimum lines are again in the vicinity of  $90^\circ$ , except in this case the average line remains at  $0^\circ$ .

Figure 11: The measured angle parameters as a function of longitude, giving their respective maximum, minimum and average values. These figures are the result of 5,439 simulations.

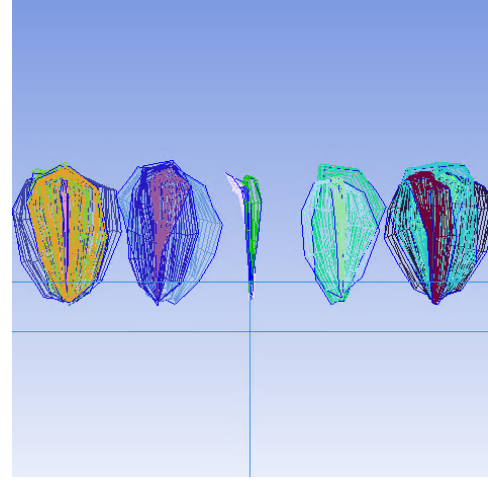
begins with a grid of 25 fractures of initial radius 800 m and separation 2 km, and then the fractures are allowed to grow to steady state as opposed to terminating after two growth steps as is the case from the quantification simulations. These models are significantly denser and more complex, with approximately 110,000 nodes and 90,000 elements, over double the complexity of the probe simulations. In Figs. 12a and 12b show the final state of a simulation with vertical fracture nuclei over the centre of the lens. The fractures show little deflection and mostly grew vertically, with some deflection that was mirrored East-to-West. The same simulation but with the network centered over the edge of the lens is presented in Figs. 12c and 12d, where increased growth is seen. The above view illustrates that one row of the network has been effectively shielded from stress by the neighbouring fractures, while the side view shows one of the outer fractures has grown significantly more than its neighbours, as stress can concentrate into one fracture's growth. Finally, Figs. 13a and 13b show the same simulation but with horizontal fracture nuclei. This leads to an increase in overlapping fractures, as well as still further East-West coverage due to more growth. The fracture growth in this case is also more uniform than with vertical fractures, with no outlier fractures.

## 5 Discussion

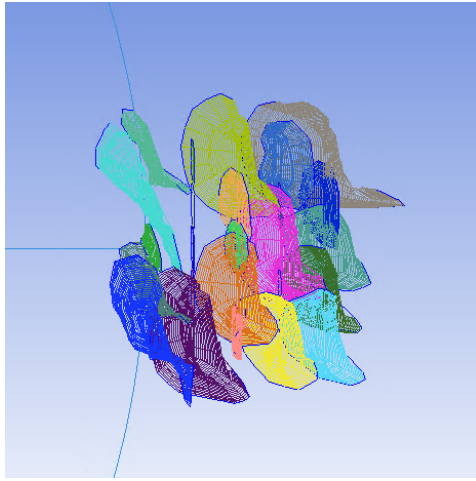
Heatmaps presented in Figs. 5a and 5b show that in a homogeneous domain, with no meltwater lens present, fractures will not preferentially grow in a horizontal orientation, and will instead tend to grow perpendicularly to the Europa surface. This result is further corroborated by the in-plane deflection quiver plots shown in Figs. 5c and 5d, where the horizontal fractures show no structure due to the lack of a conducive environment for fracture development. This is consistent with the assumption that lineae are fractures within the ice that intersect the Europa surface (Helfenstein & Parmentier, 1983).



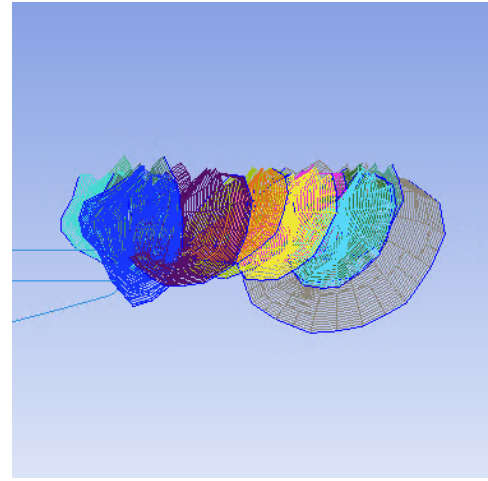
(a) Vertical fracture nuclei at the centre of the lens from above. Note the lack of significant deflection, though what deflection there is increased in the South and is East-West symmetric.



(b) Vertical fracture nuclei at the centre of the lens from the side. Again note the limited deflection.



(c) Vertical fracture nuclei at the edge of the lens from above. There is significantly increased fracture growth compared to in the centre.



(d) Vertical fracture nuclei at the edge of the lens from the side. Note the pronounced lean of the fractures that aligns with the lens, as well as the dominant growth of one fracture.

Figure 12: Networks of 25 fractures with an initial radius of 800m and a centre-to-centre separation of 2 km with varying initial orientations and locations with respect to the lens. The lens is centred at 30°N 100°E, a location of heightened stress.

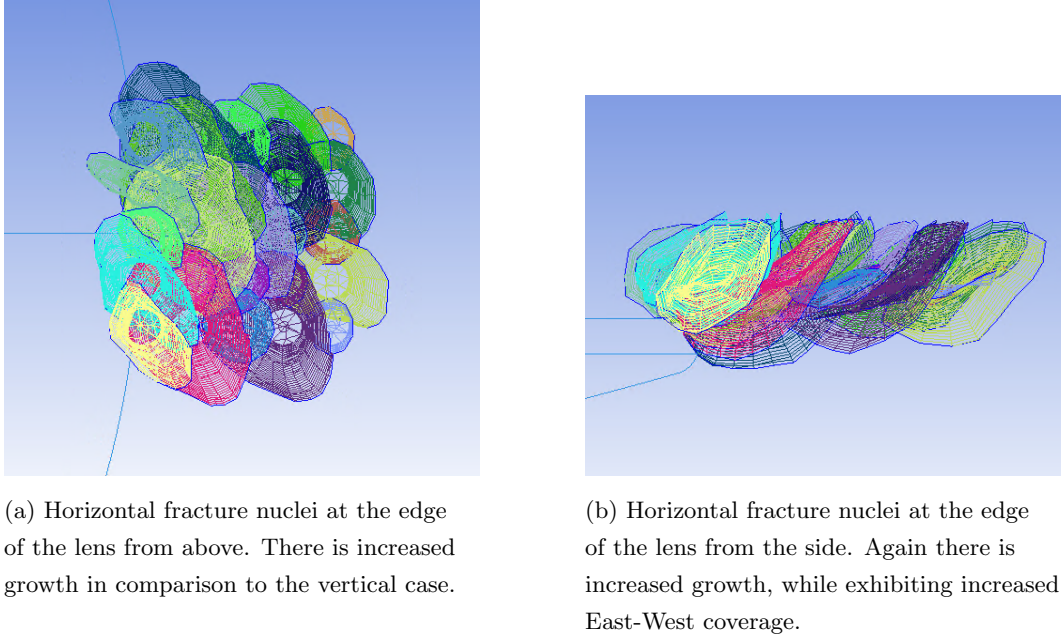


Figure 13: Networks of 25 fractures with an initial radius of 800m and a centre-to-centre separation of 2 km with varying initial orientations and locations with respect to the lens. The lens is centred at 30°N 100°E, a location of heightened stress.

Results in Fig. 8b imply that in the vicinity of a lens, fractures will preferentially grow horizontally, within the ice, as opposed to towards the surface, as observed in the homogeneous domain simulations. This supports the earlier results presented by Walding et al. (2024), further contributing to the hypothesis that the presence of these parallel fractures in proximity to a lens may weaken the ice matrix above, leading to fragmentation.

The longitudinal plots for the two angles,  $\phi$  and  $\psi$ , exhibit no visible structured behaviour with a varying longitude, as seen in Figs. 11a and 11b. In both cases, the maximum and minimum lines remain close to  $\pm 90^\circ$  which is the maximum allowed deflection, indicating that there will always be at least one fracture with a high deflection. However, the average  $\phi$  deflection hovers around  $10^\circ$  to  $20^\circ$ , this shows unified in-plane deflection, where fractures align with the overall stress field. The average  $\psi$  deflection is less pronounced and is in the vicinity of  $0^\circ$ , showing that the bulk of fractures remain horizontal. The remaining parameters all yield substantial peaks around  $0^\circ$ E and  $100^\circ$ E, with  $K_I$  among the SIFs being both the highest value overall and also exhibiting the most pronounced peak. Around  $40$ - $60^\circ$ E and  $140$ - $160^\circ$ E, the three SIFs get the closest in magnitude, indicating increased fragmentation and fracture network complexity in these regions. These peaks and valleys directly correlate with the regions between the stress concentrations seen in Fig. 1, whereas the areas of closest magnitude correlate to the stress concentrations themselves.

Across the presented heatmaps, there is a clear increase in stress around the rim of the subsurface lens, therefore leading to increased fracture growth in these regions. This may lead to separation of the ice overlaying the lens from the overall ice matrix, resulting in something similar to a calving event for a terrestrial ice sheet (Benn & Åström, 2018). Some preliminary further work exploring this effect is presented in Fig. 14, where

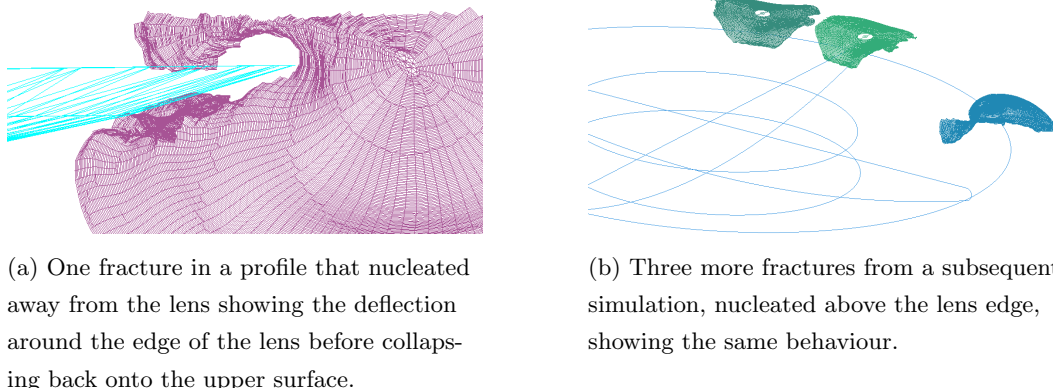


Figure 14: Two simulations both showing fractures growing around a well-defined subsurface meltwater lens.

individual fractures can be seen curving over the lens edge, while both touching the outer Europa surface as well as touching the lens body. This constitutes total mechanical separation in this region.

Figs. 12 and 13 qualitatively show the additional fracture growth that occurs at the edge of the lens. The final overall form of the fracture networks is largely independent of the initial fracture orientation for the shown cases, consistent with simulations of fracture growth in rocks (Paluszny & Matthäi, 2009). This indicates that, for sufficiently small initial fracture radii, initial fracture orientation is qualitatively of insubstantial impact on the final results. These factors combined lend strong support to the theory that the presence of subsurface meltwater lenses is likely to lead to the nucleation of chaos terrain on the surface.

The results seen in Fig. 10 show that longitude has a first order effect on the stress concentration felt by fractures, with strong spatial heterogeneity. This is conducive to fracture growth, and would also lead to differences in fracture networks across the surface. The form of the parameters against longitude further imply that there would be greater chaos formation around each quarter turn around the moon, starting from the subjovian point, although the current understanding of meltwater lens distribution is not yet refined enough to make this assertion.

## 6 Conclusions

The simulations presented in this work have investigated fracture formation in the ice on the Jovian moon Europa, specifically how fractures behave in the vicinity of subsurface meltwater lenses. This investigation has used a tidal stress model paired with a three-dimensional finite element method fracture simulator in order to model fracture development at a high degree of resolution.

The authors contend that the scientific implications of these simulations are that subsurface meltwater lenses are likely to be the nuclei above which chaos terrain forms. However, further study of individual fractures at the edge of the lens that exhibit the lipping phenomenon is warranted, as these fractures may potentially play a significant role in initial chaos formation. Work on this topic is ongoing.

## 469 7 Open Research

470 The software used in this work consists of the Imperial College Geomechanics Toolkit  
 471 (Paluszny & Matthäi, 2009), as well as a tidal stress model based upon SatStress (Wahr  
 472 et al., 2009). The executable is available at [https://github.com/waldingjc/Europa\\_meltwater\\_lenses](https://github.com/waldingjc/Europa_meltwater_lenses).  
 473 The batch files to run the simulator, the raw output data used in this work and the vi-  
 474 sualisation scripts are also available at the same repository. The data contained therein  
 475 will be archived in the National Geoscience Data Centre (NGDC) (<https://www.bgs.ac.uk/geological->  
 476 [data/national-geoscience-data-centre/](https://www.bgs.ac.uk/geological-data-national-geoscience-data-centre/)) operated by the British Geological Survey upon  
 477 paper acceptance, with the associated DOI and relevant information shared here. This  
 478 work also uses ANSYS ICEM CFD 2022 R2 (ANSYS Inc., 2022) for meshing and Rhinoceros3D  
 479 (McNeel et al., 2010) for visualisation and geometry construction.

## 480 Acknowledgments

481 This work was funded by the Royal Society through fellowship URF\R\221050 and award  
 482 RGF\R1\181016.

## 483 References

- 484 ANSYS Inc. (2022). Icem cfd 2022 r2.
- 485 Archinal, B., Acton, C., A'hearn, M., Conrad, A., Consolmango, G., Duxbury, T.,  
 486 ... others (2018). Report of the iau working group on cartographic coordinates  
 487 and rotational elements: 2015. *Celestial Mechanics and Dynamical Astronomy*,  
 488 130, 1–46.
- 489 Ashkenazy, Y. (2019). The surface temperature of europa. *Heliyon*, 5(6), e01908.
- 490 Bayer, T., Bittner, M., Buffington, B., Dubos, G., Ferguson, E., Harris, I., ... Laslo,  
 491 N. (2019). Europa clipper mission: Preliminary design report. In *2019 ieee  
 492 aerospace conference* (p. 1-24).
- 493 Becker, H. N., Lunine, J. I., Schenk, P. M., Florence, M. M., Brennan, M. J.,  
 494 Hansen, C. J., ... Alexander, J. W. (2023). A complex region of europa's  
 495 surface with hints of recent activity revealed by juno's stellar reference  
 496 unit. *Journal of Geophysical Research: Planets*, 128(12), e2023JE008105.  
 497 (e2023JE008105 2023JE008105)
- 498 Benn, D. I., & Åström, J. A. (2018). Calving glaciers and ice shelves. *Advances in  
 499 Physics: X*, 3(1), 1513819.
- 500 Billings, S. E., & Kattenhorn, S. A. (2005). The great thickness debate: Ice shell  
 501 thickness models for europa and comparisons with estimates based on flexure  
 502 at ridges. *Icarus*, 177(2), 397-412. (Europa Icy Shell)
- 503 Bills, B. G. (2005). Free and forced obliquities of the galilean satellites of jupiter.  
 504 *Icarus*, 175(1), 233–247.
- 505 Bland, M. T., Weller, L. A., Archinal, B. A., Smith, E., & Wheeler, B. H. (2021).  
 506 Improving the usability of galileo and voyager images of jupiter's moon europa.  
 507 *Earth and Space Science*, 8(12), e2021EA001935.
- 508 Burns, J. A., Matthews, M. S., et al. (1986). *Satellites* (No. 77). University of Ari-  
 509 zona Press.
- 510 Carr, M. H., Belton, M. J., Chapman, C. R., Davies, M. E., Geissler, P., Greenberg,  
 511 R., ... others (1998). Evidence for a subsurface ocean on europa. *Nature*,  
 512 391(6665), 363–365.
- 513 Cassen, P., Reynolds, R. T., & Peale, S. (1979). Is there liquid water on europa?  
 514 *Geophysical Research Letters*, 6(9), 731–734.
- 515 Collins, G., & Nimmo, F. (2009). Chaotic terrain on europa. *Europa*, 259–281.
- 516 Collins, G. C., III, J. W. H., Pappalardo, R. T., & Spaun, N. A. (2000). Evaluation  
 517 of models for the formation of chaotic terrain on europa. *Journal of Geophys-  
 518 ical Research: Planets*, 105(E1), 1709-1716.

- Cook, R. D., et al. (2007). *Concepts and applications of finite element analysis*. John Wiley & Sons.
- Craft, K. L., Patterson, G. W., Lowell, R. P., & Germanovich, L. (2016). Fracturing and flow: Investigations on the formation of shallow water sills on Europa. *Icarus*, 274, 297–313.
- Di Paolo, F., Cosciotti, B., Lauro, S. E., Mattei, E., Pettinelli, E., & Bruzzone, L. (2022, March). Melt Detection Beneath Chaos Terrains on Europa Using Ice Penetrating Radar. In *53rd lunar and planetary science conference* (Vol. 2678, p. 1395).
- Figueredo, P., Chuang, F., Rathbun, J., Kirk, R., & Greeley, R. (2002). Geology and origin of Europa's "mitten" feature (Murias Chaos). *Journal of Geophysical Research: Planets*, 107(E5), 2–1.
- Gammon, P., Kieft, H., Clouter, M., & Denner, W. (1983). Elastic constants of artificial and natural ice samples by Brillouin spectroscopy. *Journal of glaciology*, 29(103), 433–460.
- Geissler, P., et al. (1998). Evidence for non-synchronous rotation of Europa. *Nature*, 391(6665), 368–370.
- Goodman, D. (1980). Critical stress intensity factor ( $k_{ic}$ ) measurements at high loading rates for polycrystalline ice. In *Physics and mechanics of ice: Symposium Copenhagen, August 6–10, 1979, Technical University of Denmark* (pp. 129–146).
- Greeley, R., Figueredo, P. H., Williams, D. A., Chuang, F. C., Klemaszewski, J. E., Kadel, S. D., ... others (2000). Geologic mapping of Europa. *Journal of Geophysical Research: Planets*, 105(E9), 22559–22578.
- Greeley, R., Sullivan, R., Klemaszewski, J., Homan, K., Head III, J. W., Pappalardo, R. T., ... others (1998). Europa: initial Galileo geological observations. *Icarus*, 135(1), 4–24.
- Greenberg, R., Geissler, P., Hoppa, G., Tufts, B. R., Durda, D. D., Pappalardo, R., ... Carr, M. H. (1998). Tectonic processes on Europa: Tidal stresses, mechanical response, and visible features. *Icarus*, 135(1), 64–78.
- Greenberg, R., Geissler, P., Tufts, B. R., & Hoppa, G. V. (2000). Habitability of Europa's crust: The role of tidal-tectonic processes. *Journal of Geophysical Research: Planets*, 105(E7), 17551–17562.
- Heggy, E., Scabbia, G., Bruzzone, L., & Pappalardo, R. T. (2017). Radar probing of Jovian icy moons: Understanding subsurface water and structure detectability in the Juice and Europa missions. *Icarus*, 285, 237–251.
- Helfenstein, P., & Parmentier, E. (1983). Patterns of fracture and tidal stresses on Europa. *Icarus*, 53(3), 415–430.
- Hoppa, G. V., Tufts, B. R., Greenberg, R., & Geissler, P. E. (1999). Formation of cycloidal features on Europa. *Science*, 285(5435), 1899–1902.
- Howell, S. M., Leonard, E., Lovelace-Sims, K., Mills, A., Senske, D., & Patthoff, D. (2021). Fomenting chaos: Formation on Europa through dry porous compaction. In *Lunar and planetary science conference* (Vol. 2548, p. 2423).
- Hussmann, H., Spohn, T., & Wieczorkowski, K. (2002). Thermal equilibrium states of Europa's ice shell: Implications for internal ocean thickness and surface heat flow. *Icarus*, 156(1), 143–151.
- Jacobson, R., Haw, R., McElrath, T., & Antreasian, P. (2000). A comprehensive orbit reconstruction for the Galileo prime mission in the J2000 system. *The Journal of the Astronautical Sciences*, 48, 495–516.
- Jaeger, J. C., Cook, N. G., & Zimmerman, R. (2009). *Fundamentals of rock mechanics*. John Wiley & Sons.
- Kargel, J. S., Kaye, J. Z., Head III, J. W., Marion, G. M., Sassen, R., Crowley, J. K., ... Hogenboom, D. L. (2000). Europa's crust and ocean: origin, composition, and the prospects for life. *Icarus*, 148(1), 226–265.

- 573 Lee, S., Pappalardo, R. T., & Makris, N. C. (2005). Mechanics of tidally driven fractures in europa's ice shell. *Icarus*, 177(2), 367-379. (Europa Icy Shell)
- 574 Lee, S., Pappalardo, R. T., & Makris, N. C. (2007). Reply to "comment on 'mechanics of tidally driven fractures in europa's ice shell'". *Icarus*, 189(2), 598-599.
- 575 Lucchitta, B. K., & Soderblom, L. A. (1982). The geology of europa. *Satellites of Jupiter*, 521-555.
- 576 Marshall, S. T., & Kattenhorn, S. A. (2005). A revised model for cycloid growth mechanics on europa: Evidence from surface morphologies and geometries. *Icarus*, 177(2), 341-366.
- 577 McKinnon, W. B. (1999). Convective instability in europa's floating ice shell. *Geophysical Research Letters*, 26(7), 951-954.
- 578 McKinnon, W. B. (2004, February). Overview of Europa's Icy Shell: Questions of Thickness, Composition, Rheology, Tectonics, and Astrobiological Potential. In P. Schenk, F. Nimmo, & L. Prockter (Eds.), *Workshop on europa's icy shell: Past, present, and future* (p. 7048).
- 579 McNeel, R., et al. (2010). Rhinoceros 3d, version 6.0. *Robert McNeel & Associates, Seattle, WA*.
- 580 Mondro, C. A., Moersch, J. E., Emery, J., & Dunne, W. M. (2023). Regional variations in observed fracture abundance and associated predictions for smaller fractures on europa with implications for regional plume origins. *Earth and Planetary Science Letters*, 602, 117928.
- 581 Moore, J. M., Asphaug, E., Sullivan, R. J., Klemaszewski, J. E., Bender, K. C., Greeley, R., ... others (1998). Large impact features on europa: Results of the galileo nominal mission. *Icarus*, 135(1), 127-145.
- 582 Nejati, M., Paluszny, A., & Zimmerman, R. W. (2015). A disk-shaped domain integral method for the computation of stress intensity factors using tetrahedral meshes. *International Journal of Solids and Structures*, 69, 230-251.
- 583 Nimmo, F. (2004). What is the young's modulus of ice? In *Workshop on europa's icy shell: Past, present, and future* (p. 7005).
- 584 Nimmo, F., Thomas, P., Pappalardo, R., & Moore, W. (2007). The global shape of europa: Constraints on lateral shell thickness variations. *Icarus*, 191(1), 183-192.
- 585 O'Brien, D. P., Geissler, P., & Greenberg, R. (2002). A melt-through model for chaos formation on europa. *Icarus*, 156(1), 152-161.
- 586 Office, U. S. N. O. N. A., Office, G. B. N. A., Science, Britain), E. R. C. G., Laboratory, R. A., for the Central Laboratory of the Research Councils (Great Britain), C., ... Office, G. B. H. (2016). *The astronomical almanac for the year ...* U.S. Government Printing Office.
- 587 Ojakangas, G. W., & Stevenson, D. J. (1989a). Polar wander of an ice shell on europa. *Icarus*, 81(2), 242-270.
- 588 Ojakangas, G. W., & Stevenson, D. J. (1989b). Thermal state of an ice shell on europa. *Icarus*, 81(2), 220-241.
- 589 Paluszny, A., & Matthäi, S. K. (2009). Numerical modeling of discrete multi-crack growth applied to pattern formation in geological brittle media. *International Journal of Solids and Structures*, 46(18), 3383-3397. Retrieved from <https://www.sciencedirect.com/science/article/pii/S0020768309002078> doi: <https://doi.org/10.1016/j.ijsolstr.2009.05.007>
- 590 Paluszny, A., & Zimmerman, R. W. (2013). Numerical fracture growth modeling using smooth surface geometric deformation. *Engineering Fracture Mechanics*, 108, 19-36.
- 591 Pappalardo, R. T., Belton, M. J., Breneman, H., Carr, M., Chapman, C. R., Collins, G., ... others (1999). Does europa have a subsurface ocean? evaluation of the geological evidence. *Journal of Geophysical Research: Planets*, 104(E10), 24015-24055.

- 627 Paris, P., & Erdogan, F. (1963, 12). A Critical Analysis of Crack Propagation Laws.  
 628     *Journal of Basic Engineering*, 85(4), 528–533.
- 629 Petrovic, J. (2003). Review mechanical properties of ice and snow. *Journal of mate-*  
 630 *rials science*, 38, 1–6.
- 631 Poinelli, M., Larour, E., Castillo-Rogez, J., & Vermeersen, B. (2019). Crevasse prop-  
 632 agation on brittle ice: Application to cycloids on europa. *Geophysical Research*  
 633 *Letters*, 46(21), 11756–11763.
- 634 Qin, R., Buck, W. R., & Germanovich, L. (2007). Comment on “mechanics of tidally  
 635     driven fractures in europa’s ice shell” by s. lee, rt pappalardo, and nc makris  
 636     [2005. *Icarus* 177, 367–379]. *Icarus*, 189(2), 595–597.
- 637 Richard, H., Fulland, M., & Sander, M. (2005). Theoretical crack path prediction.  
 638     *Fatigue & fracture of engineering materials & structures*, 28(1-2), 3–12.
- 639 Richard, H., Schramm, B., & Schirmeisen, N.-H. (2014). Cracks on mixed mode  
 640     loading—theories, experiments, simulations. *International Journal of Fatigue*,  
 641     62, 93–103.
- 642 Rudolph, M. L., & Manga, M. (2009). Fracture penetration in planetary ice shells.  
 643     *Icarus*, 199(2), 536–541.
- 644 Schenk, P. M. (2002). Thickness constraints on the icy shells of the galilean satel-  
 645     lites from a comparison of crater shapes. *Nature*, 417(6887), 419–421.
- 646 Schmidt, B., Blankenship, D., Patterson, G., & Schenk, P. (2011). Active formation  
 647     of ‘chaos terrain’ over shallow subsurface water on europa. *Nature*, 479(7374),  
 648     502–505.
- 649 Schulze-Makuch, D., & Irwin, L. N. (2001). Alternative energy sources could support  
 650     life on europa. *Eos, Transactions American Geophysical Union*, 82(13), 150–  
 651     150.
- 652 Sieme, D., & Rezaei-Ghaleh, N. (2024). Water dynamics in eutectic solutions of  
 653     sodium chloride and magnesium sulfate: implications for life in europa’s sub-  
 654     surface ocean and ice shell. *Phys. Chem. Chem. Phys.*, 26, 105–115.
- 655 Sinha, N. K. (1989). Elasticity of natural types of polycrystalline ice. *Cold regions*  
 656 *science and technology*, 17(2), 127–135.
- 657 Thomas, R. N., Paluszny, A., & Zimmerman, R. W. (2020). Growth of three-  
 658     dimensional fractures, arrays, and networks in brittle rocks under tension and  
 659     compression. *Computers and Geotechnics*, 121, 103447.
- 660 Turtle, E., & Ivanov, B. (2002). Numerical simulations of impact crater excavation  
 661     and collapse on europa: Implications for ice thickness. In *Lunar and planetary*  
 662 *science conference* (p. 1431).
- 663 Van Hoolst, T., Rambaux, N., Karatekin, Ö., Dehant, V., & Rivoldini, A. (2008).  
 664     The librations, shape, and icy shell of europa. *Icarus*, 195(1), 386–399.
- 665 Vilella, K., Choblet, G., Tsao, W.-E., & Deschamps, F. (2020). Tidally heated  
 666     convection and the occurrence of melting in icy satellites: Application to eu-  
 667     ropa. *Journal of Geophysical Research: Planets*, 125(3), e2019JE006248.  
 668     (e2019JE006248 10.1029/2019JE006248)
- 669 Wahr, J., Selvans, Z. A., Mullen, M. E., Barr, A. C., Collins, G. C., Selvans, M. M.,  
 670     & Pappalardo, R. T. (2009). Modeling stresses on satellites due to nonsyn-  
 671     chronous rotation and orbital eccentricity using gravitational potential theory.  
 672     *Icarus*, 200(1), 188–206.
- 673 Walding, J. C., Paluszny, A., & Zimmerman, R. W. (2024). Numerical modelling  
 674     of the influence of tidal stresses on fracture patterns on the surface of europa.  
 675     *Rock Mechanics and Rock Engineering*, 1–18.
- 676 Walker, C. C., Bassis, J. N., & Schmidt, B. E. (2021). Propagation of vertical frac-  
 677     tures through planetary ice shells: the role of basal fractures at the ice–ocean  
 678     interface and proximal cracks. *The Planetary Science Journal*, 2(4), 135.
- 679 Witasse, O. (2020). *Juice (jupiter icy moon explorer): a european mission to explore*  
 680 *the emergence of habitable worlds around gas giants* (Tech. Rep.). Copernicus  
 681 Meetings.